Digest Journal of Nanomaterials and Biostructures Vol. 19, No. 4, October-December 2024, p. 1371-1381

Exploring the structural, morphology, optical and magnetic properties of $ZnCo_xMn_{(2-x)}O_4$ prepared using hydrothermal method

B. Mahalakshmi [a], L. Balakrishnan [b,*], S. Esakki Muthu [c], J. Sahadevan [d]
[a]*Department of Physics, Hindusthan College of Engineering and Technology, Coimbatore, India-641021*
[b] *Department of Physics, Government College of Technology, Coimbatore - 641 013, India*
[c] *Centre for Materials Science, Department of Physics, Faculty of Arts Science Commerce and Management, Karpagam Academy of Higher Education, Coimbatore, India-641 021*
[d] *Centre for Biophotonics and Technology, Department of Biomedical Engineering, Karpagam Academy of Higher Education, Coimbatore, India -641 021*

Here we report the structural and physical property of $ZnCo_xMn_{(2-x)}O_4$ (x = 0, 0.1 and 0.2) materials. The hierarchical $ZnCo_xMn_{2-x}O_4$ (x = 0, 0.1 and 0.2) have been successfully synthesized by hydrothermal method. The surface of the $ZnCo_xMn_{(2-x)}O_4$ varies according to its composition which is investigated. The absorption and band gap of the material were measured by UV-Vis diffuse reflectance spectroscopy (DRS) in the range of 200 – 800 nm. It was observed that the band gap gets decreased from the parent compound. The room temperature photoluminescence emission spectra of $ZnCo_xMn_{(2-x)}O_4$ (x = 0,0.1 and 0.2) has been investigated. The magnetic property of material shows an antiferromagnetic nature. Further, X-ray photoelectron spectroscopy analysis confirms the substitution of Co on Mn site.

(Received June 24, 2024; Accepted September 24, 2024)

Keywords: Nanoparticles, Structural, Nanoflakes, Optical, Photoluminescence, Antiferromagnetism

1. Introduction

Due to their unique characteristics, which include catalytic, optical, magnetic, and electrical capabilities, spinel ferrite magnetic nanoparticles have garnered a lot of attention in recent years [1–5]. They may find use in several industries, including medication delivery, high density storage media, electromagnetic absorbers, microwave devices, catalysis, sensors, water purification, antimicrobial, nanoelectronics, and magnetic resonance imaging [6–8]. Spinel – type Cobalt doped Zinc Manganese Oxide [$ZnCo_xMn_{(2-x)}O_4$], possess tetragonally biased structure at room temperature. As viable, ZnMn2O4 has provoked plenty of benefits because of its many remarkable qualities, including its magnetic behaviour, photocatalytic activity, electrochemical performance, etc [3–7] with ample application in high capacity energy storage and minimum cost. Particle size, morphologies, and composite structure of nanostructures largely amplify their physical, chemical, and dielectric capabilities [8]. The doping of $ZnMn_2O_4$ with rare earth metal ominously changes the surface morphology of the material. By modifying the composition of the material, it shows significant changes in the morphology of the material. As initially reported $ZnMn_2O_4$ nanowire counterfeited by thermal evaporation technique [9], and consecutive nano flower grouping [10] and hierarchical pore hollows $ZnMn_2O_4$ nanotube [11] were attained by number of methods, which revealed a prevailing advancement on definite surface area and performance. The cubic like $ZnMn_2O_4$ showes a promising photo-catalytic activity towards pollutants [9].

* Corresponding author: bslv85@gmail.com
https://doi.org/10.15251/DJNB.2024.194.1371

The growth of $ZnMn_2O_4$ hollow microspheres by $ZnMn_2O_4$ nano sized building blocks provides the aids of nanometer sized assembly ensures good structural stability and cyclability as an anodic material for lithium – ion batteries [10]. In our work, we report the hydrothermal methods for the synthesis of Tetragonal – $ZnMn_2O_4$ nanoparticle using deionized water as a solvent and metal nitrates as solute. It is an excellent option for high-performance lithium-ion batteries, which are widely used in portable devices, electric cars, and energy storage systems because of its high specific capacity and outstanding cycling stability [12–17]. In this study, we have described a synthesis methodology for $ZnCo_xMn_{2-x}O_4$ nanoparticles by hydrothermal method [18–20]. The present paper deals on the research of structural, morphological, optical and magnetic characteristics of $ZnMn_2O_4$ with varied doping composition.

2. Materials and experimental method

The $ZnCo_xMn_{(2-x)}O_4$ (x = 0, 0.1 and 0.2), to prepare proportion by hydrothermal synthesis, the metal precursors zinc nitrate hexahydrate ($Zn(NO_3)_2.6H_2O$), cobalt nitrate hexahydrate ($Co(NO_3)_2.6H_2O$) and manganese nitrate tetrahydrate ($Mn(NO_3)_2.4H_2O$) are dissolved in 80 ml deionized water and stirred for several hours, then an alkaline solution of sodium hydroxide (NaOH) is added to the solution until pH reaches ~11, along with NH_4OH for hydrolysis. The chemical reagent has high purity level (99.9%) added drop wise under stirring to adjust the pH of the solution to around 11-12. After that, the mixture is put in an autoclave lined with teflon and heated to 140°C for 12 hours. After the hydrothermal reaction, the resulting powder is washed thoroughly with ethanol and deionized water for several times to remove any residual impurities or by products. After several hours, the dried sample is calcinated at 500^0 C in muffle furnace for 4 h. When the calcinations process gets done, the samples were fine powdered using mortar and pestle. The phase cleanliness of the sample has been verified by the X-ray diffraction (XRD) techniques; the morphology of the sample is identified by scanning electron microscopy (SEM). The optical properties of the materials are studied through UV-Vis (DRS) and photoluminescence spectroscopy.

3. Results and discussion

3. 1. The structural property

From the XRD patterns of $ZnCo_xMn_{(2-x)}O_4$ (x = 0, 0.1 and 0.2), it has been seen that the intensities of (1 1 2), (1 0 3) and (2 1 1) diffraction peaks are relatively strong which shows the samples have good crystallinity nature. The XRD graph of $ZnCo_xMn_{(2-x)}O_4$ (x = 0, 0.1 and 0.2) are shown in Fig. 1 (Left). The ZCMO samples (x = 0, 0.1 and 0.2) shows a single phase and tetragonal structure with a lattice constant of a = 0.5272 nm, b = 0.5272 nm and c = 0.9426 nm and space group of $I4_1/amd$. These are consistent with the standard card JCPDS No.: 77-0470. The existence of a small quantity of ZnO phase can be observed in doped ZMO through two reflections at 31.9° and 45.6° (highlighted in red). On doping Co in ZMO, the low-concentration dopant has some mixed structure of ZnO, and the higher concentration has a slight structural variation, as reported in the literature [21,22]. The crystallite size was estimated using Scherer formula,

$$D=\frac{k\lambda}{\beta cos\theta}$$

where D is the crystalline size, K is the shape factor, λ the X-ray wavelength, θ the Bragg's angle in radian, and β is the full width at half maximum. The lattice parameters are calculated and the values are given in Table 1. Using Debye Scherer's formula, the average crystalline size is determined to be 28 nm for x = 0, 19 nm for x = 0.1 and 10 nm for x = 0.2. The high intensity peak of ZCMO (x = 0, 0.1, and 0.2) is magnified in Fig. 1b (right), where the peak shift with increased dopant concentration is clearly visible. As increasing the concentration of Co dopant in $ZnMn_2O_4$, the peaks get broaden and shifted towards lower angle which is due to lattice expansion.

Table 1. The crystalline size and lattice parameter of pure and Co – doped sample.

Composition	Crystalline Size $D = \frac{0.9\lambda}{\beta cos\theta}$	Lattice Parameter (Å)		
		a (nm)	b (nm)	c (nm)
$ZnMn_2O_4$	28.52 nm	0.5715	0.5715	0.9136
$ZnCo_{0.1}Mn_{1.9}O_4$	21.30 nm	0.5718	0.5718	0.9138
$ZnCo_{0.2}Mn_{1.8}O_4$	10 nm	0.5717	0.5717	0.9136

Table 2. The coercive field, Magnetization and remnant magnetization of $ZnMn_2O_4$, $ZnCo_{0.1}Mn_{1.9}O_4$ and $ZnCo_{0.2}Mn_{1.8}O_4$.

Composition	H_C (T)	M (emu/g) @ 300 K	M_R (emu/g)
$ZnMn_2O_4$	0.0016	3.21	0.0143
$ZnCo_{0.1}Mn_{1.9}O_4$	0.004	2.66	0.0114
$ZnCo_{0.2}Mn_{1.8}O_4$	0.0052	1.51	0.0086

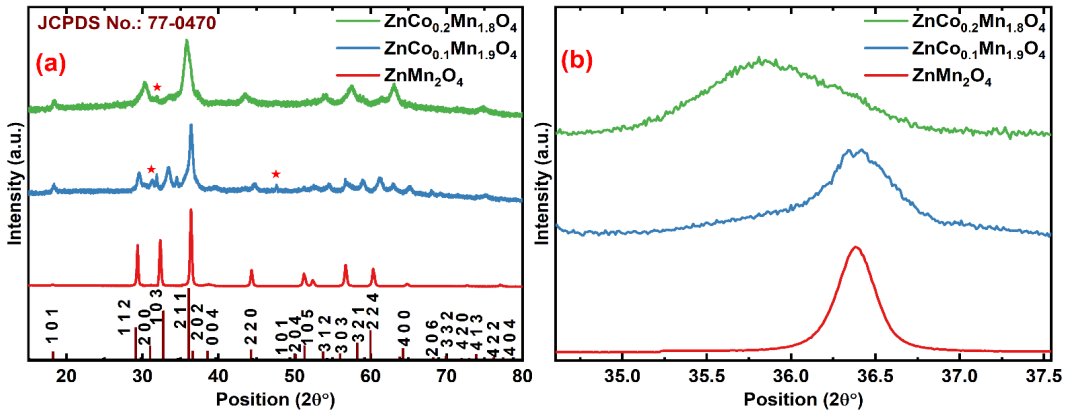

Fig. 1. X- ray diffraction pattern of the synthesized sample for $ZnCo_xMn_{(2-x)}O_4$ (x = 0, 0.1 and 0.2).

3.2. The surface morphology

The SEM images in Fig. 2 reveal the size distribution and homogeneous microstructure of ZMO and ZCMO surface morphologies. In Fig. 2a and b, SEM micrographs of ZnMn2O4 depict uniform-sized nano flakes. Intriguingly, the introduction of Co transforms the microstructure from flakes to spheres, although some nano flakes persist, as illustrated in Fig. 2e. With higher Co concentrations, this morphological shift becomes more uniform, signifying increased stability in ZMO. The average size of ZCMO spheres measures 273 nm. EDAX spectra confirm the presence of constituent elements, with weight and atomic percentages aligning well, as depicted in Fig. 2c, f, and i.

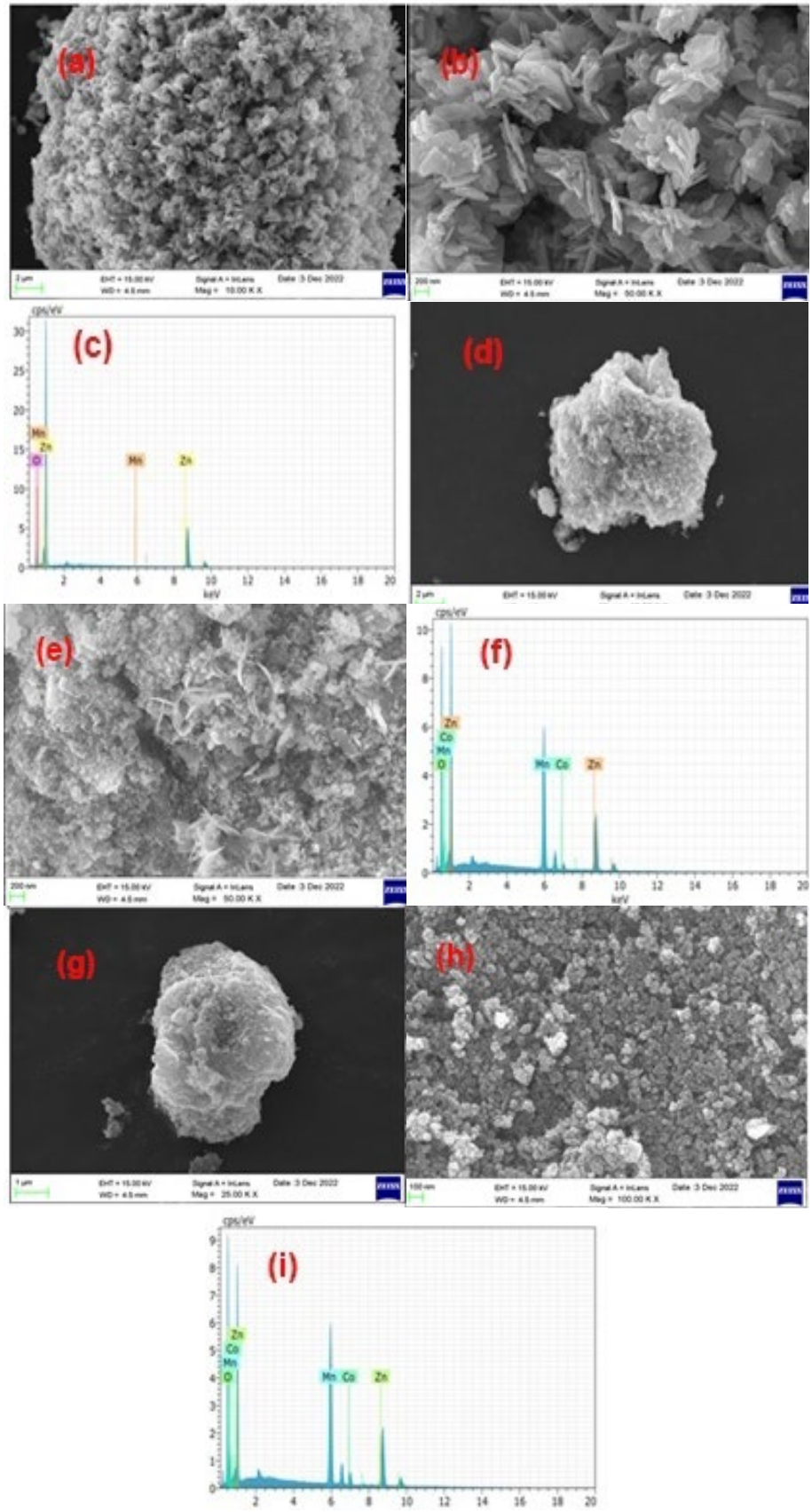

Fig. 2. (a, b) SEM images of $ZnMn_2O_4$, (d, e) $ZnCo_{0.1}Mn_{1.9}O_4$ and (g, h) $ZnCo_{0.2}Mn_{1.8}O_4$and (c) EDAX spectra for $ZnMn_2O_4$, (f) EDAX spectra for $ZnCo_{0.1}Mn_{1.9}O_4$ and (i) EDAX spectra for $ZnCo_{0.2}Mn_{1.8}O_4$.

3.3. Ultra-violet- visible diffuse reflectance spectroscopy (UV-Vis DRS)

The optical property for $ZnCo_xMn_{(2-x)}O_4$ was substantiated mostly by the absorption behaviour of the material. The absorption spectra for $ZnMn_2O_4$, $ZnCo_{0.1}Mn_{1.9}O_4$ and $ZnCo_{0.2}Mn_{1.8}O_4$were around 200 – 370 nm, 370 – 600 nm and 380 – 680 nm as shown in Fig 3a. The band gap of $ZnCo_xMn_{(2-x)}O_4$ (x = 0, 0.1 and 0.2) were measured based on the Tauc's relation and the graph were fitted according to the Kubelka – Munk function, $\alpha h\nu = A\,(h\nu - Eg)^2$. Where α, the absorption coefficient of matterials, hν is the incident photons energy, A is a constant, and E_g is called as material's optical band gap. By Kulbelka – Munk function the band gaps for $ZnMn_2O_4$, $ZnCo_{0.1}Mn_{1.9}O_4$ and $ZnCo_{0.2}Mn_{1.8}O_4$ were determined as 3.72 eV, 3.25 eV and 3.29 eV as shown in the Fig. 3 (b to d). By observing the band gaps of each material, it is an insulator or dielectric material.

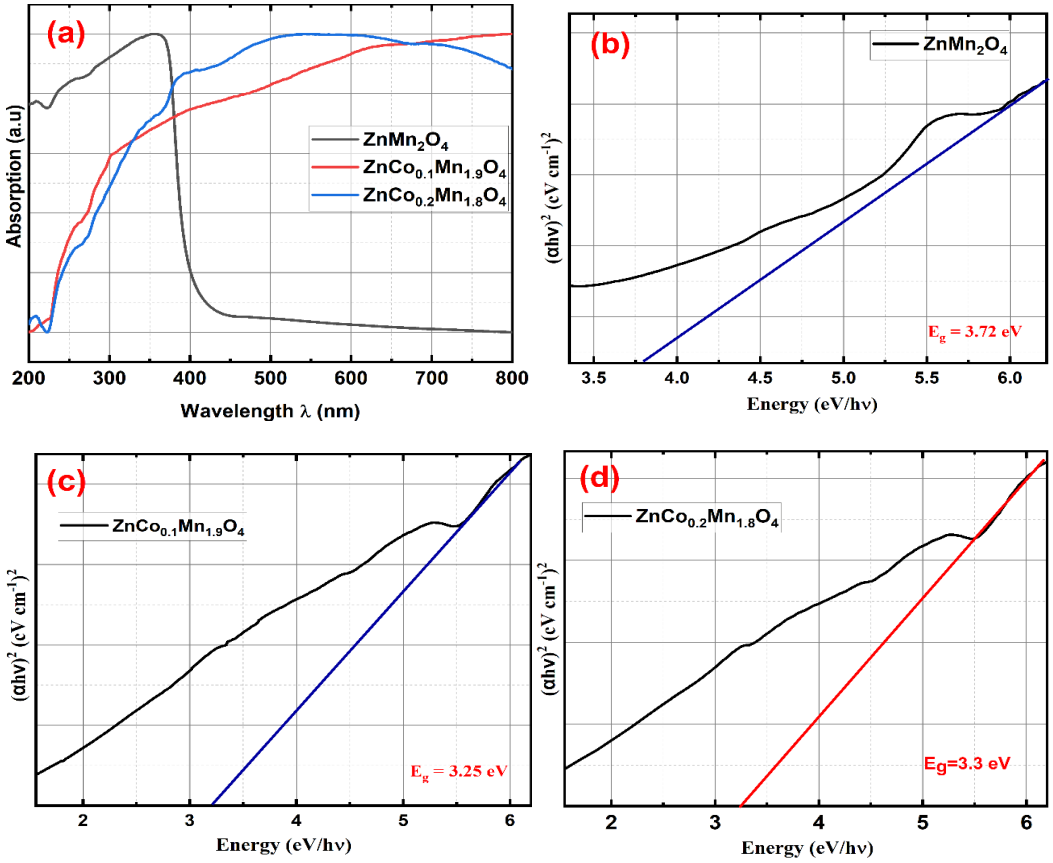

Fig. 3. (a) UV-vis absorption spectra for $ZnCo_xMn_{(2-x)}O_4$ (x = 0,0.1and 0.2), (b), (c) and (d) Band gap for $ZnMn_2O_4$, $ZnCo_{0.1}Mn_{1.9}O_4$ and $ZnCo_{0.2}Mn_{1.8}O_4$.

3.4. Photoluminescence studies

The photoluminescence (PL) spectroscopy was used to study the luminescence characteristics and recombination phenomena of the materials. Fig.4 (a and b) displays the deconvoluted photoluminescence spectra for $ZnMn_2O_4$and $ZnCo_{0.1}Mn_{1.9}O_4$ under excitation wavelength of 300 nm. For $ZnMn_2O_4$ a strong visible emission occurred at 469 nm and 557 nm respectively. The Co doped $ZnMn_2O_4$, shows the ultraviolet peak at 344 nm and 388 confirms the photo generated electron and holes in the UV region. The strong visible peak occurs at 464 and 554 nm. The deconvoluted PL spectra fitted with a Gaussian line shape in the entire spectrum range shows 5 components for the $ZnMn_2O_4$ sample and 6 components for the $ZnCo_{0.1}Mn_{1.9}O_4$ sample. Sample $ZnMn_2O_4$ exhibits five PL bands in the Indigo-blue-green emissions while the $ZnCo_{0.1}Mn_{1.9}O_4$ exhibit UV, indigo-blue-green emissions. The apparent peak in the visible

spectrum for both samples indicate the presence of defects of oxygen vacancies, originating from the distorted lattice of $ZnMn_2O_4$ [23,24]. Blue-green emission peaks up monotonically while UV emission demines somewhat as doping is increased. As a result, the fitting results indicate that 5 and 6 PL components, which exhibit distinct trends with increasing doping concentration, can be used to characterize the PL spectra.

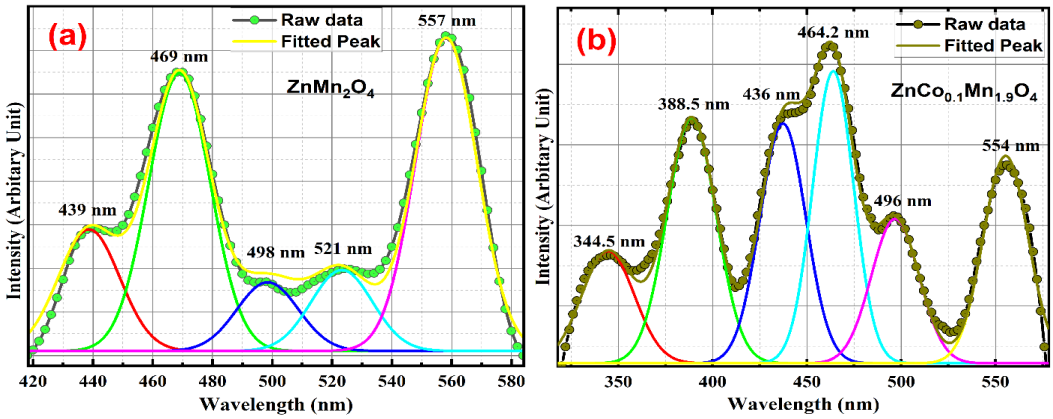

Fig. 4. (a, b) Deconvoluted PL spectra of $ZnMn_2O_4$ and $ZnCo_{0.1}Mn_{1.9}O_4$

3.5. X-ray photoelectric spectroscopy

In order to analyse the chemical condition of $ZnCo_xMn_{(2-x)}O_4$ (x = 0 (ZMO) and 0.2 (ZCMO)) samples, X-ray photoelectron spectroscopy (XPS) is utilized and the survey spectrum is given in Fig 5 and Fig 6. The XPS survey spectrum of parent ZMO is depicted in Figure 5 (a) which validates the existence of the constituent elements Zn, O and Mn. Similarly, the XPS survey spectrum depicted in Figure 6 (a) validates the existence of the constituent elements Zn, Co, O, and Mn (in a 10 wt% Co-doped ZMO sample) by identifying their individual binding energies. The valence states of the constituent elements are validated by their corresponding core-level XPS spectra. The XPS spectrum of the O 1s orbital has a wide and asymmetrical shape, suggesting the existence of oxygen species consisting of many components. The O 1s peaks observed in both ZMO and ZCMO provide additional evidence that the presence of Co influences the development of defective spinel oxide.

Figures 5 (b) and 6 (b) show three different peaks in both the ZMO and ZCMO O 1s peaks. The O 1s peak was observed at 530.96, 532.54, and 534.41 eV on the surface of ZMO. The dominant signal at 530.95 eV can be explained by the existence of O^{2-} ions originating from the surface lattice oxygen. When adsorbed OH- species (C-OH) or chemisorbed oxygen (O-) are present, the peak at 530.9 eV will appear, which creates a vacancy on the surface for oxygen [25]. The signal observed at 532.6 eV indicates the presence of superoxide (O^{2-}) production. The researchers have attributed the adsorption of water by the materials to a value of 534.41 eV [26]. The peaks with greater width at higher binding energies pose a more intricate challenge when it comes to interpretation in the oxide system. Incorporating Co into the Mn lattice site reduces the intensity of the bulk oxide peak at approximately 531.05 eV. This occurs due to the generation of additional oxygen vacancies in conjunction with surface imperfections. This promotes a greater concentration of peroxide/superoxide ions, resulting in prominent peaks at around 533.16/534.9 eV. When oxygen vacancies occur, oxygen species migrate between the bulk oxides and the surface oxides. The oxidation states of $Co^{3+/2+}$ are elevated in the ZCMO [27]. The ZMO has integrated peak areas of 63.8%, 34.8%, and 1.4%, while the ZCMO has integrated peak areas of 39.7%, 40.3%, and 19.9%, respectively. We computed the binding energies of the O1s peaks in ascending order. The increased peak width, accounting for 39.7% of the total peak area, indicates a higher concentration of oxygen deficit in ZCMO nanoparticles. The Gaussian XPS peak fit deconvoluted the broad (approximately 6.37 eV (ZMO) and 10 eV (ZCMO)) O 1s spectra resulting in a superposition of three components. Incorporating Co in Mn site broadens O 1s core

level spectra. The Zn 2p core level spectra of ZMO and ZCMO are splitted into two spin states which is shown in Figure 5 (c) and 6 (c) respectively. The Zn 2p binding energies in ZMO are approximately 1045 eV and 1022 eV, corresponding to the Zn $2p_{1/2}$ and Zn $2p_{3/2}$ peaks, respectively, indicating the valence state of Zn^{2+} [28,29]. Similarly, the binding energy of ZCMO are slightly shifted towards higher binding energy side, which are 1045.25 eV and 1022.23 eV. The binding energy width between to spin state are approximately 23 for both the spectra of ZMO and ZCMO samples. The Mn 2p XPS spectrum of ZCMO is obviously different from that of the pristine electrode (Figures 5 (d) and 6 (d). There are two major peaks with binding energies of 655.34 eV and 641.83 eV for ZMO and 642.03 eV and 653.60 eV for ZCMO, corresponding to Mn $2p_{3/2}$ and Mn $2p_{1/2}$, respectively. Mn^{3+} states are associated with the peaks at low binding energies, while Mn^{4+} states are responsible for the peaks at high binding energies [30]. On doping ZMO with Co, the Mn^{3+} peak of Mn $2p_{3/2}$ deceases and Mn $2p_{1/2}$ increases. Similarly, the Mn^{4+} peak of Mn $2p_{3/2}$ increases, and Mn $2p_{1/2}$ decreases. The widths between the two spin states $2p_{3/2}$ and $2p_{1/2}$ of ZMO and ZCMO are 13.51 and 11.57 eV, respectively [31,32].

Figure 5 (e) shows the distinct core-level Co 2p spectra of co-doped $ZnMnO_3$. Deconvoluting and fitting the core-level XPS spectra of Co becomes challenging due to the reduced intensity of the Co $2p_{1/2}$ peak, but the Co $2p_{3/2}$ peak remains distinctly observable. The spin orbit doublet Co $2p_{3/2}$ peak is separated into two distinct peaks at 781.1 eV and 786.8 eV. These peaks correspond to the Co^{3+} $2p_{3/2}$ and Co^{2+} $2p_{3/2}$ configurations, respectively [33]. Substituting Co with Mn results in a narrowing and lowering of the Mn 2p peak, indicating the presence of multiple excitations and the simultaneous existence of $Mn^{3+/4+}$ states. The absence of satellite peaks provides additional confirmation for both low-spin Co3+ and high-spin Co2+ ions to be present [34,35].

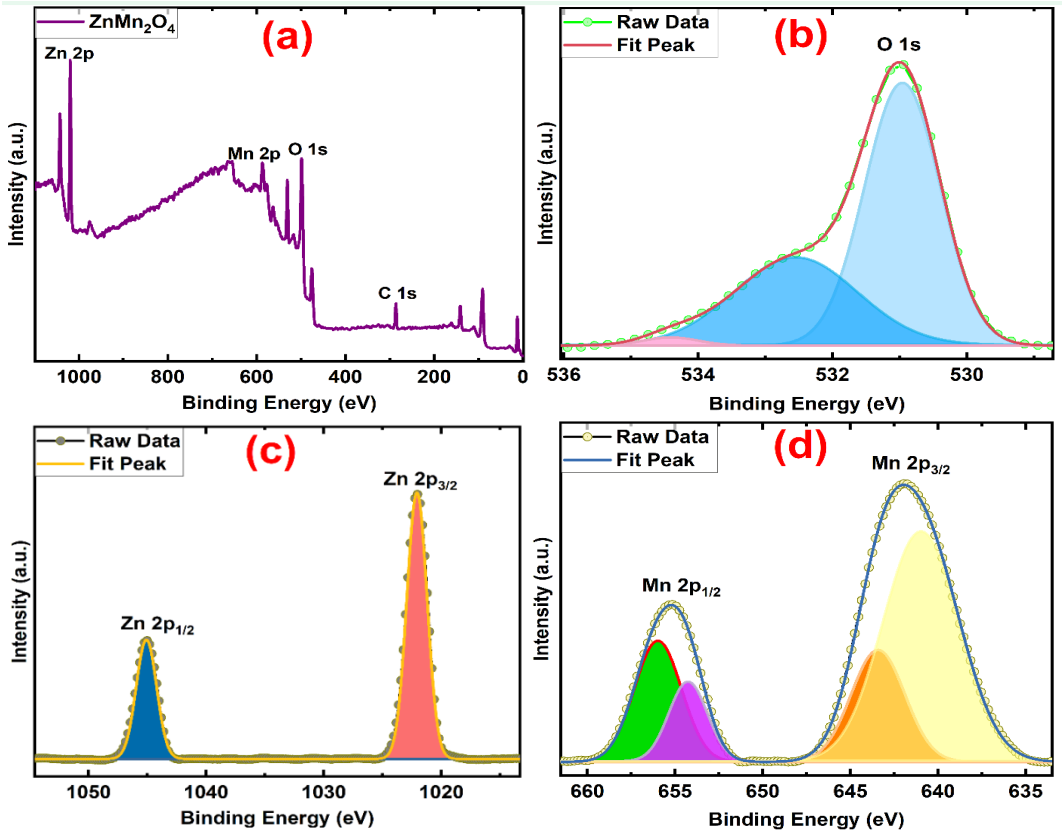

Fig. 5. XPS spectra of a) full spectra of $ZnMn_2O_4$ b) core level of O1s c) core level of Zn 2p level d) core level of Mn 2p level.

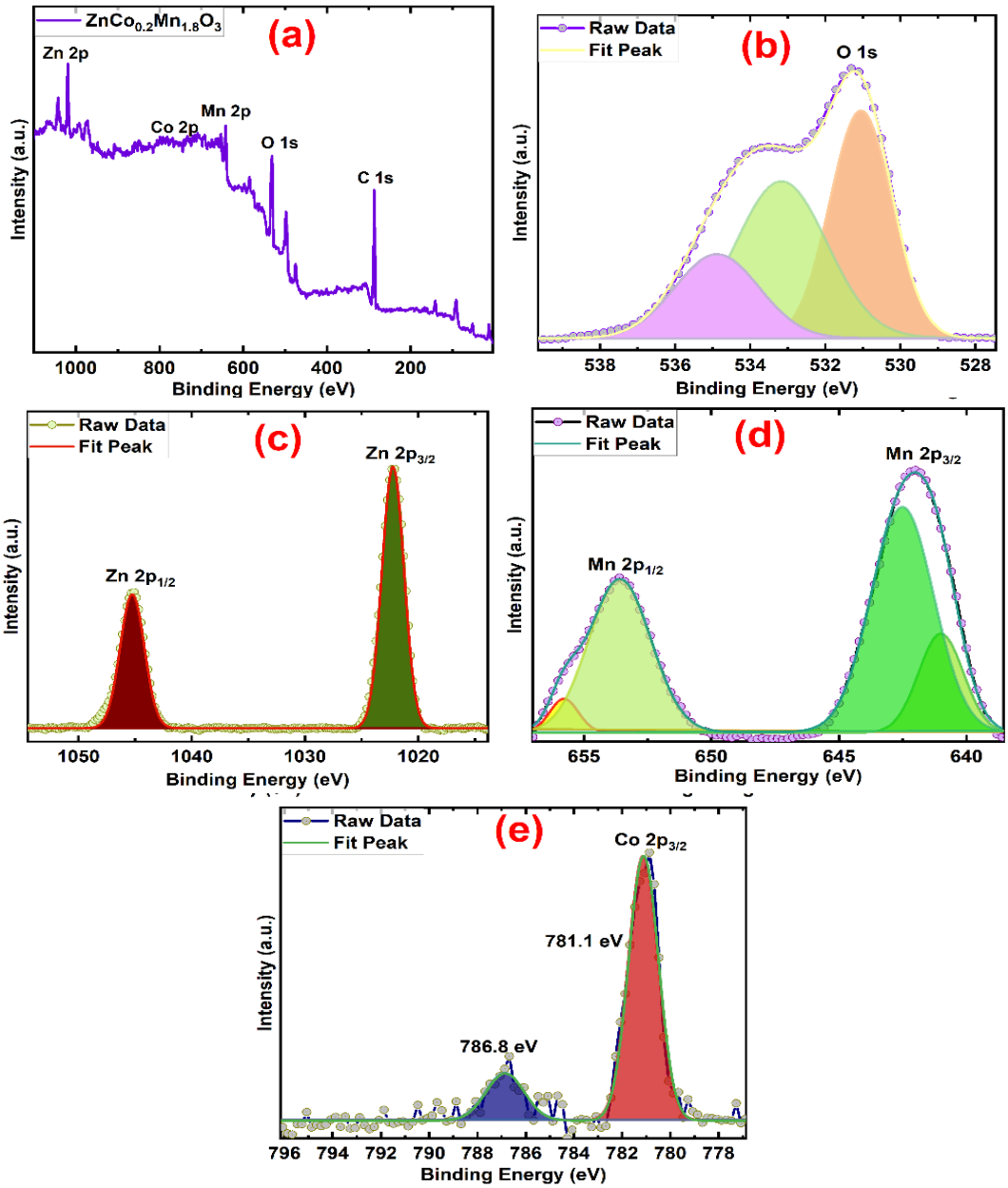

Fig. 6. XPS spectra of a) full spectra of $ZnCo_{0.2}Mn_{1.8}O_4$ b) core level of O1s c) core level of Zn 2p level d) core level of Mn 2p level e) core level of Co 2p level.

3.6. Magnetic studies

To understand the magnetic property of samples at 300 K, the isothermal magnetization has been measured (M-H) for a field change from -2.5 T to 2.5 T and shown in Fig 7. The M-H loop at 300 K clearly shows that the magnetization decreases with the increase of content and also the magnetization didn't saturate at the maximum field applied. The inset of figure shows the magnified view of M-H curve to see the hysteresis clearly. The hysteresis loop for $ZnMn_2O_4$is large compared with $ZnCo_{0.1}Mn_{1.9}O_4$ and $ZnCo_{0.2}Mn_{1.8}O_4$. The magnetic nature of $ZnMn_2O_4$ can be attributed to the antiferromagnetism and this behavior reduces with the increase of Co in Mn. The similar behavior of M-H for $ZnMn_2O_4$was reported earlier [36–38]. The values of magnetization (M_S), remnant magnetization (M_R) and coercive field (H_C) has been calculated from the MH curve and are given in Table. 2. The H_C decreases with the increase of Co, whereas the M_R and M_S decrease. These suggest that the magnetic nature for parent $ZnMn_2O_4$to Co doped $ZnMn_2O_4$ changes from soft magnetic to hard magnetic.

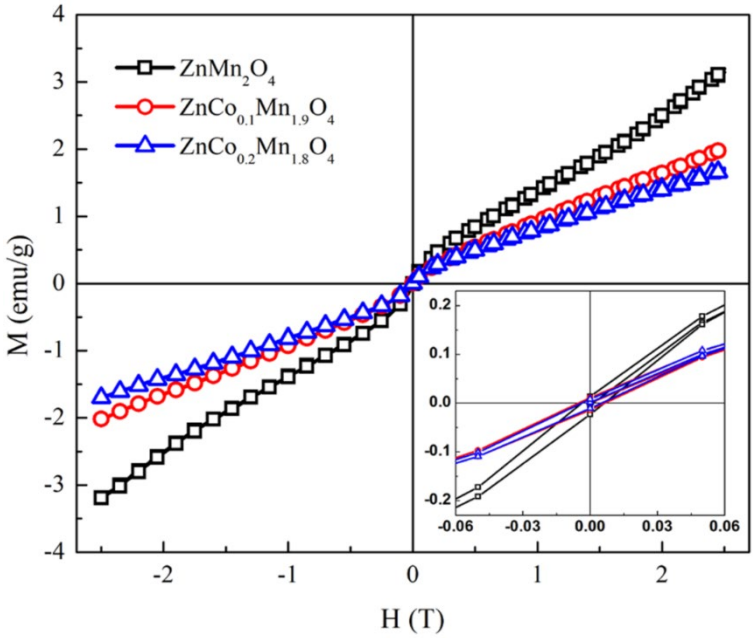

Fig. 7. M-H Curve of $ZnMn_2O_4$, $ZnCo_{0.1}Mn_{1.9}O_4$ and $ZnCo_{0.2}Mn_{1.8}O_4$ at room temperature.

4. Conclusion

Cobalt doped zinc manganese oxide has been successfully synthesized by hydrothermal method. The obtained material was characterized by XRD, SEM, UV-Vis DRS and PL. The crystalline structure for $ZnCo_xMn_{(2-x)}O_4$ was measured by X- Ray Diffraction analysis and confirm the high crystalline nature of the material. The decrease in band gap confirms the material has good light absorbent property. The morphology of parent $ZnMn_2O_4$ shows uniformly sized nanoflakes structure, and when Co is added to ZMO, the microstructure is rebuilt from flakes to spherical structure. The broadening of excitons transition of $ZnCo_xMn_{(2-x)}O_4$ from visible to UV area, as displayed in the PL spectra, can be used to confirm it. The magnetic property of sample at room temperature indicates the antiferromagnetic nature of the sample with increasing coercive field.

References

[1] G. Singhal, R. Bhavesh, K. Kasariya, A.R. Sharma, R.P. Singh, Journal of Nanoparticle Research. 13 (2011) 2981–2988; https://doi.org/10.1007/S11051-010-0193-Y/METRICS.

[2] J. Guo, R. Wang, W.W. Tjiu, J. Pan, T. Liu, J Hazard Mater. 225–226 (2012) 63–73; https://doi.org/10.1016/J.JHAZMAT.2012.04.065.

[3] H. Nouri, A. Habibi-Yangjeh, M. Azadi, J Photochem Photobiol A Chem. 281 (2014) 59–67; https://doi.org/10.1016/J.JPHOTOCHEM.2014.03.006.

[4] N. Guo, X.Q. Wei, X.L. Deng, X.J. Xu, Appl Surf Sci. 356 (2015) 1127–1134. https://doi.org/10.1016/J.APSUSC.2015.08.185.

[5] L. Zhou, H. Bin Wu, T. Zhu, X.W. Lou, J Mater Chem. 22 (2011) 827–829; https://doi.org/10.1039/C1JM15054E.

[6] G. Zhang, L. Yu, H. Bin Wu, H.E. Hoster, X.W. Lou, Advanced Materials. 24 (2012) 4609–4613; https://doi.org/10.1002/ADMA.201201779.

[7] S.M. Disseler, Y. Chen, S. Yeo, G. Gasparovic, P.M.B. Piccoli, A.J. Schultz, Y. Qiu, Q. Huang, S.W. Cheong, W. Ratcliff, Scientific Reports. 2015 5:1 5 (2015) 1–9; https://doi.org/10.1038/srep17771.

[8] J. Tang, J. Li, Y. Cheng, P. Huang, Q. Deng, Vacuum. 120 (2015) 96–100; https://doi.org/10.1016/J.VACUUM.2015.06.001.
[9] M. Mehta, A.P. Singh, S. Kumar, S. Krishnamurthy, B. Wickman, S. Basu, Vacuum. 155 (2018) 675–681; https://doi.org/10.1016/J.VACUUM.2018.05.052.
[10] T. Zhang, H. Yue, H. Qiu, K. Zhu, L. Zhang, Y. Wei, F. Du, G. Chen, D. Zhang, RSC Adv. 5 (2015) 99107–99114; https://doi.org/10.1039/C5RA16667E.
[11] Y. Bessekhouad, D. Robert, J. V. Weber, Catal Today. 101 (2005) 315–321; https://doi.org/10.1016/J.CATTOD.2005.03.038.
[12] P. Zhang, X. Li, Q. Zhao, S. Liu, Nanoscale Res Lett. 6 (2011) 1–8; https://doi.org/10.1186/1556-276X-6-323/FIGURES/7.
[13] C. Chen, S. Cao, W. Yu, X. Xie, Q. Liu, Y. Tsang, Y. Xiao, Vacuum. 116 (2015) 48–53; https://doi.org/10.1016/J.VACUUM.2015.02.031.
[14] A. Sahoo, Y. Sharma, Mater Chem Phys. 149–150 (2015) 721–727; https://doi.org/10.1016/J.MATCHEMPHYS.2014.11.032.
[15] D. Ding, M. Long, W. Cai, Y. Wu, D. Wu, C. Chen, Chemical Communications (2009) 3588–3590; https://doi.org/10.1039/B903865E.
[16] J.P. Chen, C.M. Sorensen, K.J. Klabunde, G.C. Hadjipanayis, E. Devlin, A. Kostikas, Phys Rev B. 54 (1996) 9288; https://doi.org/10.1103/PhysRevB.54.9288.
[17] J.B. Goodenough, K.S. Park, J Am Chem Soc. 135 (2013) 1167–1176; https://doi.org/10.1021/JA3091438/ASSET/IMAGES/MEDIUM/JA-2012-091438_0009.GIF.
[18] F.M. Courtel, H. Duncan, Y. Abu-Lebdeh, I.J. Davidson, J Mater Chem. 21 (2011) 10206–10218; https://doi.org/10.1039/C0JM04465B.
[19] M. Kruk, M. Jaroniec, Chemistry of Materials. 13 (2001) 3169–3183; https://doi.org/10.1021/CM0101069/ASSET/IMAGES/MEDIUM/CM0101069N00001.GIF.
[20] K.M. Shaju, F. Jiao, A. Débart, P.G. Bruce, Physical Chemistry Chemical Physics. 9 (2007) 1837–1842; https://doi.org/10.1039/B617519H.
[21] L. V. Saraf, P. Nachimuthu, M.H. Engelhard, D.R. Baer, J Sol-gel Sci Technol. 53 (2010) 141–147; https://doi.org/10.1007/s10971-009-2067-2.
[22] J. Jaćimović, Z. Micković, R. Gaál, R. Smajda, C. Vâju, A. Sienkiewicz, L. Forró, A. Magrez, Solid State Commun. 151 (2011) 487–490; https://doi.org/10.1016/j.ssc.2010.12.025.
[23] Z.K. Heiba, M.B. Mohamed, N.M. Farag, S.I. Ahmed, Journal of Materials Science: Materials in Electronics. 32 (2021) 22718–22729; https://doi.org/10.1007/S10854-021-06757-X/METRICS.
[24] X.Q. Wei, N. Guo, G.X. Wang, X.R. Ma, Appl Phys A Mater Sci Process. 125 (2019) 1–9; https://doi.org/10.1007/S00339-019-2956-3/METRICS.
[25] H. Liang, Y. Hong, C. Zhu, S. Li, Y. Chen, Z. Liu, D. Ye, Catal Today 201 (2013) 98–102; https://doi.org/10.1016/J.CATTOD.2012.04.036.
[26] E. Rattigan, Z. Sun, T. Gallo, M. Angel Nino, S. de Oliveira Parreiras, C. Martín-Fuentes, J. Carlos Martin-Romano, D. Écija, C. Escudero, I. Villar, J. Rodríguez-Fernández, J. V Lauritsen, Phys. Chem. Chem. Phys. 24 (2022) 9236-9246; https://doi.org/10.1039/D2CP00399F.
[27] X. Jiang, Y. Dong, Z. Zhang, J. Li, J. Qian, D. Gao, J Alloys Compd. 878 (2021) 160433; https://doi.org/10.1016/J.JALLCOM.2021.160433.
[28] X. Su, J. Huang, B. Yan, Z. Hong, S. Li, B. Pang, Y. Luo, L. Feng, M. Zhou, Y. Xia, RSC Adv. 8 (2018) 31388-31395; https://doi.org/10.1039/c8ra05871g.
[29] D. Xu, D. Fan, W. Shen, Nanoscale Res Lett. 8 (2013) 1–9; https://doi.org/10.1186/1556-276X-8-46/FIGURES/7.
[30] J. Sahadevan, M. Radhakrishnan, N. Padmanathan, S. Esakki Muthu, P. Sivaprakash, M. Kadiresan, Materials Science and Engineering: B. 284 (2022) 115875; https://doi.org/10.1016/j.mseb.2022.115875.
[31] S. Diodati, A. Minelli, P. Dolcet, S. Gross, Surface Science Spectra. 22 (2015) 1–20; https://doi.org/10.1116/11.20141103.
[32] M. Wang, K. Chen, J. Liu, Q. He, G. Li, F. Li, Catalysts. 8 (2018) 138;

https://doi.org/10.3390/CATAL8040138.
[33] M. Smyrnioti, T. Ioannides, M. Smyrnioti, T. Ioannides, Cobalt. (2017); https://doi.org/10.5772/INTECHOPEN.70947.
[34] N.S. Mcintyre, D.D. Johnston, L.L. Coatsworth, R.D. Davidson, J.R. Brown, Surface and Interface Analysis. 15 (1990) 265-272; https://doi.org/10.1002/sia.740150406.
[35] H. Wang, W. Xu, S. Richins, K. Liaw, L. Yan, M. Zhou, H. Luo, Electrochim Acta. 296 (2019) 945–953; https://doi.org/10.1016/j.electacta.2018.11.075.
[36] P. Patra, I. Naik, H. Bhatt, S.D. Kaushik, Physica B Condens Matter. 572 (2019) 199–202; https://doi.org/10.1016/J.PHYSB.2019.08.005.
[37] H. Li, B. Song, W.J. Wang, X.L. Chen, Mater Chem Phys. 130 (2011) 39–44; https://doi.org/10.1016/J.MATCHEMPHYS.2011.04.072.
[38] H. Štěpán, S. Zdeněk, N. Ladislav, J. Ondřej, Š. Petr, S. David, M. Miroslav, Ceramics-Silikáty. 57 (2013) 162 – 166.